

Article

Multifunctional Chitosan/Xylan-Coated Magnetite Nanoparticles for the Simultaneous Adsorption of the Emerging Contaminants Pb(II), Salicylic Acid, and Congo Red Dye

Hebatullah H. Farghal ^{1,*}, Marianne Nebsen ² and Mayyada M. H. El-Sayed ^{1,*}

¹ Department of Chemistry, School of Sciences and Engineering, The American University in Cairo, AUC Avenue, P.O. Box 74, New Cairo, Cairo 11835, Egypt

² Analytical Chemistry Department, Faculty of Pharmacy, Cairo University, Kasr-El Aini Street, Cairo 11562, Egypt

* Correspondence: hebatullahfarghal@aucegypt.edu (H.H.F.); mayyada@aucegypt.edu (M.M.H.E.-S.)

Abstract: In this work, we develop chitosan/xylan-coated magnetite (CsXM) nanoparticles as eco-friendly efficient adsorbents for the facile removal of contaminants from water. Characterization of CsXM using Fourier Transform Infra-Red (FTIR) Spectroscopy, Scanning Electron Microscopy (SEM), X-Ray Diffraction (XRD), Thermogravimetric Analysis (TGA), Transmission Electron Microscopy (TEM), Zeta potential measurements, and Brunauer-Emmet-Teller (BET) analysis, confirmed the successful preparation of a chitosan/xylan complex coated over magnetite, which is characterized by being mesoporous, thermally stable and of neutral charge. Three contaminants, Pb(II), salicylic acid (SA), and congo red (CR), were chosen as representative pollutants from three major classes of contaminants of emerging concern: heavy metals, pharmaceuticals, and azo dyes. Pb(II), SA, and CR at initial concentrations of 50 ppm were removed by 64.49, 62.90, and 70.35%, respectively, on applying 6 g/L of CsXM. The contaminants were successfully removed in ternary systems, with Pb(II) and SA being more competitive in their adsorption than CR. Adsorption followed the Freundlich isotherm model and the pseudo-second order kinetic model, while the binding was suggested to occur mainly via chemical chelation for Pb(II) and physical interaction for SA and CR, which demonstrates the multifunctional potential of the nanoparticles to capture different contaminants regardless of their charge.

Keywords: emerging contaminants; complexation; chitosan; xylan; magnetite nanoparticles



Citation: Farghal, H.H.; Nebsen, M.; El-Sayed, M.M.H. Multifunctional Chitosan/Xylan-Coated Magnetite Nanoparticles for the Simultaneous Adsorption of the Emerging Contaminants Pb(II), Salicylic Acid, and Congo Red Dye. *Water* **2023**, *15*, 829. <https://doi.org/10.3390/w15040829>

Academic Editors: P. V. Nidheesh and Alessandro Erto

Received: 20 January 2023

Revised: 15 February 2023

Accepted: 16 February 2023

Published: 20 February 2023



Copyright: © 2023 by the authors. Licensee MDPI, Basel, Switzerland. This article is an open access article distributed under the terms and conditions of the Creative Commons Attribution (CC BY) license (<https://creativecommons.org/licenses/by/4.0/>).

1. Introduction

Emerging contaminants are a class of pollutants that have been recently detected in water streams with the aid of sophisticated analytical instruments but have not yet been consistently monitored or properly treated in wastewater treatment plants. One major concern with these contaminants is the lack of regulatory frameworks that control their levels despite the health threats they pose to humans and living organisms when they accumulate in water bodies. In addition to the newly discovered contaminants that fall under various groups of pharmaceuticals, personal care products, flame retardants, and pesticides [1], there are legacy contaminants that have been present for a long time; yet concerns about their hazards are still emerging. One of these contaminants is the heavy metal lead (Pb II), which is commonly used in plumbing systems and paints. It is considered an emerging contaminant due to its persistence in the environment, with detection levels exceeding 15 ppb in drinking water, and its alarming toxicity, which could possibly harm the nervous system of children and lower their IQ, as well as affect fetal growth in pregnant women [2,3]. Pb(II) has been found at a concentration of 35 mg/L in the wastewater of a metal manufacturing factory located in Sishuan, China [4], and at 3 mg/L in the wastewater of a storage battery factory in Ankara, Turkey [5]. Another interesting emerging contaminant is the

pharmaceutical salicylic acid (SA). It is a Non-Steroidal Anti-Inflammatory Drug (NSAID) that has been found in effluent wastewater at a concentration of 0.452 µg/L [6], and also at 27.8 mg/L in North American wastewater treatment plants [7]. SA showed intermediate acute toxicity to *Daphnia magna* and *Daphnia longispina*, with chronic exposures affecting normal reproduction or growth [8]. A third emerging contaminant of concern is the azo-dye Congo red (CR). The annual global production of azo-dyes is estimated to be over 70% of the approximate total production (one million tons) of all dyes [9], of which 10–15% is released into wastewater [10], giving rise to wastewaters with high total dissolved solids, biological oxygen demand, and chemical oxygen demand [11]. Azo-dyes can cause dermatitis, allergies, and mutations in human beings as well as prevent light transfer to photosynthesis-based living organisms, thus threatening human life and the ecosystem [12,13]. The concentration of CR, in particular, has reached about 60 ppm in textile wastewater [14].

Several methods have been implemented for the removal of heavy metals and emerging contaminants; these include flocculation and coagulation, ion exchange, reverse osmosis, membrane filtration, and advanced oxidation processes [15,16]. Of the facile, efficient, and cost-effective methods for the removal of emerging contaminants is adsorption [17–21]. In view of the global trends and Sustainable Development Goals (SDGs)—set by the United Nations—which address the sustainable use of natural resources, there has been a growing interest in utilizing biopolymers as eco-friendly adsorbent materials [22]. Chitosan and xylan are two popular biopolymers that exist abundantly in a variety of natural resources since chitosan exists in the supporting material of crustaceans and insects, while xylan is a main component of plant hemicellulose. Chitosan is a partially deacetylated chitin that consists mainly of β -(1→4)-2-amino-2-deoxy-D-glucose units as the deacetylated units, along with the acetylated units of β -(1→4)-2-acetamido-D-glucose. Its chemical and physical properties vary with its molecular weight, crystallinity, and deacetylation degree. Xylan, on the other hand, is a pentose heteropolymer sugar formed of a chain of xylose units linked by β -1,4 bonds and substituted with uronic acid and arabinose [23,24]. Chitosan and xylan are characterized by their biodegradability, safety, availability, and cost-effectiveness [25]. Chitosan nanocomposites have been deployed in the adsorption studies of several emerging contaminants. Chitosan grafted with 2-(Methacryloyloxy)ethyl]dimethyl-(3-sulfopropyl)ammonium hydroxide (MEDSP) has been successful in removing SA with a maximum adsorption capacity of 89 mg/g at 30 °C and pH 4 [26]. In addition, the nanocomposite of chitosan with montmorillonite clay adsorbed 54.52 mg/g of CR at 30 °C and pH 7 [27], while its nanocomposite with hydroxyapatite completely removed Pb(II) from aqueous solution when 2 g/L of the nanocomposite was applied on 100 ppm of Pb(II) at pH 5.6 [28]. As for xylan-based adsorbents, there have been no reports on their removal for SA or CR; however, their potential for adsorbing several heavy metals such as copper and zinc [29,30], and dyes such as ethyl violet, has been reported [31]. Combining chitosan with xylan is advantageous in forming an amide bond complex between the primary amine of chitosan and the glucuronic acid of xylan [32,33] or possibly a Schiff base formed upon the reaction of the primary amine in chitosan with the aldehydic group of xylan to obtain what is known as imine or azomethine group, which could form stable metal complexes with Pb(II) via coordination [34]. Schiff bases, in general, can form complexes with almost all metals and have anti-bacterial and anti-cancer effects [35]. In addition, chitosan and xylan structures have abundant OH groups that could possibly be efficient in capturing organic contaminants by H-bonding.

Thus, our work aimed to prepare chitosan/xylan amide complex and possibly a Schiff base, then coat it over magnetite to ease its separation from water by a magnetic field. Formulating chitosan/xylan nanocomposite in the form of magnetic nanoparticles (CsXM) has not been, to the best of our knowledge, reported elsewhere. The prepared CsXM nanoparticles were characterized for their physico-chemical and textural properties and then tested for their potential to adsorb Pb(II), SA, and CR as examples for three important classes of contaminants of high concern: namely, heavy metals, pharmaceuticals, and dyes.

Adsorption was tested under two different sets of initial concentrations: the higher range of concentrations represented the concentrations in industrial effluents while the lower range represented surface water concentrations. The nanoparticles were applied at high doses in one adsorption step or at half these doses in two steps, so as to avoid possible adsorbent aggregation at high doses, as well as eliminate mass transfer effects that can arise when larger agitated vessels are used and which would reduce the adsorption efficiency. Additionally, the adsorption equilibrium and kinetics were studied, the regeneration of the adsorbent was investigated, and the mechanism of adsorption was discussed. Finally, adsorption was examined in the ternary systems of the three contaminants and compared to adsorption in single systems.

2. Materials and Methods

2.1. Materials

Chitosan of high molecular weight (MW 310,000–375,000 Da, 75% degree of deacetylation) was purchased from Sigma Aldrich, Iceland, while xylan containing 12.8% glucuronic acid was bought from Neogen Megazyme Corporation, Bray, Ireland. For magnetite precursors, ferrous sulfate heptahydrate (98%) was purchased from Alfa Aesar (Erlenbachweg, Germany), while anhydrous ferric chloride (97%), and sodium hydroxide pellets (97%) were purchased from Fisher Scientific (Loughborough, UK). For the emerging contaminants, Pb (II) acetate trihydrate (99%) was supplied by Adwic Company (Qalubia, Egypt), while salicylic acid extra pure (99%) and congo red were purchased from Loba Chemie (Mumbai, India). Solvents such as hydrochloric acid (37%) were obtained from Acros Organics, Germany, ethyl alcohol absolute (99.8%) from Fisher (Hampton, NH, USA), and glacial acetic acid (99.8%) from Advent (Maharashtra, India).

2.2. Synthesis of CsXM, CsM, and XnM

Dissolution of xylan was carried out using the method provided by Neogen Megazyme Corp. (Ireland) where a mass of 1 g of xylan was dispersed in 4 mL of 95% ethyl alcohol C_2H_5OH (*v/v*), then completed to 49 mL with distilled water and left to stir till boiling takes place. Once boiled, the heater was turned off and the solution was left to stir boiling for 10 min. Afterward, the solution was cooled down to room temperature (25 ± 2 °C) and a volume of 1 mL acetic acid CH_3COOH (99.8%) was added. A weight of 0.25 g of chitosan was then added while stirring for 8 h. The final concentrations of xylan and chitosan were 2% *w/v* and 0.5% *w/v*, respectively.

For magnetite preparation (Fe_3O_4), the co-precipitation method was applied, where masses of 1.50 g of ferrous sulfate heptahydrate ($FeSO_4 \cdot 7H_2O$) and 1.75 g of anhydrous ferric chloride ($FeCl_3$) were dissolved in 20 mL of distilled water and were left to shake for 20 min. A 30% (*w/v*) NaOH solution was then added dropwise while shaking until the solution turned black. This was then placed on a shaker heated to 70 °C and left shaking for 30 min. The formed magnetite was separated by magnetic decantation and washed with distilled water three times. The preparation of magnetite was confirmed by TEM and XRD, as shown in Figures S2a and S2c of SI, respectively. The band gap energy of magnetite was estimated to be 2.67 eV at 464 nm, which is comparable to values reported in previous literature, 1.97–2.2 eV [36,37]. The band gap energy (E) was calculated using the equation $E = hc/\lambda$; h is Planck's constant, λ is the wavelength, and c is the speed of light [38].

To prepare CsXM, 1 g of the magnetite slurry was suspended in 25 mL of distilled water by stirring. A volume of 5 mL of the chitosan/xylan composite was added dropwise over the stirring magnetite solution. The solution was left to stir for 13 h then poured on a petri dish until it dried out after 1 day under air. The formed nanocomposites were washed 7 times with distilled water and left to dry, after which the obtained flakes were sieved on a 500- μm sieve. Concentrations of xylan and chitosan in CsXM nanocomposite were 0.33% *w/v* and 0.083% *w/v*, respectively.

Regarding chitosan-coated magnetite (CsM) and xylan-coated magnetite (XnM) preparation, the same above procedures were applied. In the case of CsM, only a chitosan

solution was prepared by adding 0.25 g of chitosan powder to 2% aqueous solution of acetic acid and kept stirring for 8 h; 5 mL of this solution was then dropped on the magnetite solution which contains 1 g of magnetite slurry dissolved in 25 mL of distilled water. For XnM, xylan solution was prepared as mentioned before via heating and cooling without chitosan and 5 mL of the solution was dropped into the magnetite slurry solution.

2.3. Characterization of CsXM, CsM, and XnM

^1H NMR (400 MHz) measurement was performed on beechwood xylan using boiled D₂O as a solvent on Bruker advance (III) model Ultra Shield NMR spectrometer, Billerica, MA, USA, to confirm the presence of acetyl groups required for a Schiff base formation. To ensure the formation of the amide bond and Schiff base, FTIR measurements were performed on CsXM using Thermo Scientific, Nicolet 380 FT-IR spectrometer (Waltham, MA, USA) in the range of 4000–500 cm^{-1} , applying the KBr disc method. Raman spectroscopy was also performed on the samples in the solid state using ProRaman-L High Performance Raman Spectrometer, Enwave optronics, Inc., Irvine, CA, USA, in the range of 1000–2000 cm^{-1} . To view the morphology of the formed nanoparticles, TEM (JEOL, JEM-2100 electron microscope, Tokyo, Japan) images were taken after sonication for 10 min, whereas SEM (Zeiss Supra 55, Oberkochen, Germany) images were taken after gold sputtering (HummerTM 8.0, Union City, CA, USA) for 3 min at 15 mA. To identify the crystal structure of the nanoparticles, XRD measurements were performed at room temperature (25 ± 2 °C) using Cu K alpha at a wavelength of 1.5406 Å and 2θ scan range of 3–70° (Bruker, Discover D-8, Billerica, MA, USA). The thermal stability of the nanoparticles was examined using TGA (Thermo Scientific, TGA Q50, Waltham, MA, USA) with a heating ramp of 10 °C/min till 750 °C under nitrogen gas. For surface charge determination, Dynamic Light Scattering (DLS) measurements were performed on the nanoparticles at several pHs using Malvern Panalytical Zetasizer Nano Series Nano-ZS90 (Malvern, UK). A Brunauer-Emmet-Teller (BET) analyzer (ASAP 2020-Micromeritics equipment, Norcross, GA, USA) was used to determine the porosity of the nanoparticles from nitrogen adsorption/desorption isotherms at 77 K after degassing the adsorbent with nitrogen gas at 50 °C for 8 h. Pore volume was estimated based on the Barrett-Joyner-Halenda (BJH) model.

2.4. Adsorption in Single Systems

Batch adsorption was conducted using a rotary shaker at 60 rpm for Pb (II), SA, and CR at initial concentrations ranging from 10 to 50 ppm, similar to those in industrial wastewater, an adsorbent dose of 0.67 g/L, and at room temperature (25 ± 2 °C). Also, adsorption was tested under a more environmentally-relevant surface water initial concentration range of 1–20 ppm, with an adsorbent dose of 1.33 g/L at 25 ± 2 °C. To prepare the stock solutions, deionized water with an initial pH of 5.5 ± 0.1 was used without pH adjustment and the contaminant was dissolved in water. The pH of the prepared solutions of Pb(II), SA, and CR was 5.5 ± 0.1 , 4.0 ± 0.3 , and 6.1 ± 0.2 , respectively. To enhance the removal performance, higher adsorbent doses were tested, ranging from 0.33 to 6 g/L at 50 ppm of each contaminant. The dose was applied in one step or split equally in two consecutive steps. The kinetics of adsorption was investigated at an initial concentration of 50 ppm and an adsorbent dose of 0.67 g/L under the same pH and temperature conditions alluded to earlier. After adsorption, the adsorbate solution was subjected to magnetic decantation and the supernatant was measured on a UV–VIS spectrometer (Pg instruments T80+ spectrometer, UK) at 296 and 511 nm for SA and CR, respectively, while the supernatant for Pb(II) was measured on an atomic absorption spectrophotometer (Spectrum SP-AA 4000 spectrometer, China). The corresponding concentrations (C_e) for the measured absorbances were calculated from a pre-prepared calibration curve and substituted in Equation (S1) (SI) [39] to determine the percent removal and Equation (S2) (SI) [40] to calculate the equilibrium adsorption capacity (q_e). The best fitting kinetic and equilibrium isotherm models were also determined according to Equations (S3)–(S8), presented in the SI [40–45].

2.5. Adsorption in Ternary Systems

Ternary system was prepared from a mixture of the tested contaminants each at an initial concentration of 50 ppm then adjusting the pH to either 5.5 or 4.0. Adsorption was carried out at a dose of 3 g/L at room temperature (25 ± 2 °C). The concentrations of the solutions after adsorption were measured spectroscopically. CR absorbance readings were obtained from the combined spectrum without manipulation. However, for SA, derivative ratio calculations were performed, and the removal was calculated based on the amplitudes of SA before and after adsorption, which were read at 275 nm. The derivative ratio was applied on the calibration curve of SA, which gave a correlation coefficient of 1. Spectra for the ternary system before adsorption at both pHs are presented in the supplementary information (Figure S6 of SI).

2.6. Regeneration

Adsorption was first performed at an initial concentration of 5 ppm, adsorbent dose of 1.33 g/L, and respective pHs of 5.5 ± 0.1 , 4.0 ± 0.3 , and 6.1 ± 0.2 for Pb(II), SA, or CR at room temperature (25 ± 2 °C). The experimental contact time was adjusted to 3 h for Pb(II), 2 h for SA, and 1 h for CR when the tested contaminants reached equilibrium. After adsorption of Pb(II), SA, or CR, CsXM nanoparticles were regenerated using 50 mL of 0.1 N HCl for 1 h in the case of Pb(II), and 50 mL of 0.1 N NaOH for 1 h and 30 min in the cases of SA and CR, respectively. The nanoparticles were then washed with 50 mL deionized water for 30 min after Pb(II) and SA regeneration and 15 min after CR regeneration. Regeneration was undertaken for 3 consecutive cycles.

2.7. Statistical Analysis

All measurements were performed in triplicate, and their respective means and standard deviations (expressed as mean \pm SD) were determined accordingly. Linear regression analysis was used to predict the equilibrium and kinetic profiles.

3. Results and Discussion

3.1. Physical and Chemical Characteristics

The NMR spectrum (Figure S1 of SI) shows a peak at 2.2 ppm confirming the presence of acetyl groups on xylan, which can possibly form a Schiff base with the primary amine of chitosan [46,47]. The FTIR spectra of chitosan, xylan, and CsXM are shown in Figure 1a. For chitosan, the peaks at 1645 and 1580 cm^{-1} pertain to the amide I and primary amine functional groups, respectively, while the band at 1646 cm^{-1} in xylan can be ascribed to the stretching vibration of glucuronic acid [48]. The shift that occurred in the 1645 cm^{-1} peak of chitosan when CsXM was formed and the disappearance of its 1580 cm^{-1} peak, in addition to the shift in the 1646 cm^{-1} xylan band to 1635 cm^{-1} , all indicate the formation of a superimposed peak corresponding to the amide or Schiff base bond. Similar findings have previously been reported for chitosan/xylan hydrogel, confirming amide bond formation [32], and chitosan/xylan/titania Schiff base [34,49]. Since the amide or Schiff baseband in FTIR could be masked by water molecules, Raman spectroscopy was performed on the nanocomposite because this technique is not sensitive to water molecules since it is a weak water scatterer [50]. As shown in Figure 1b, the amide I, II, and III bands in CsXM appeared at about 1694, 1560, and 1322 cm^{-1} , respectively [51,52], while the very weak band at 1590 cm^{-1} in chitosan corresponded to the amine groups [53]. The multi-peak region in the range of 1300–1500 cm^{-1} in xylan could correspond to the acetyl and methyl-glucuronated groups, while in chitosan it could be assigned to the bending vibrations of CH, CH₂, and OH [53,54]. Furthermore, the change in the intensity of the OH bands when CsXM was formed compared to chitosan or xylan could be attributed to a possible hydrogen bonding between the two biopolymers. As for the band at 563 cm^{-1} in CsXM, it indicated the presence of Fe-O in magnetite [55]. This was further confirmed by XRD measurements (Figure S2c of SI) which revealed peaks with 2θ values of 30.5, 35.6, 46.8, 53.4, 57.4, 62.9°, corresponding to (202), (311), (313), (422), (511), (404) indices as per the

magnetite card 96–151-3302; this indicated a cubic crystal system, which shifted in CsXM (Figure S2d of SI) to 36.2, 41.9, 43.4, 49.9 and 63.2°, probably because the polymer induced the scattering of the penetrated X-rays, as previously reported for polypyrrole-coated magnetite [56,57].

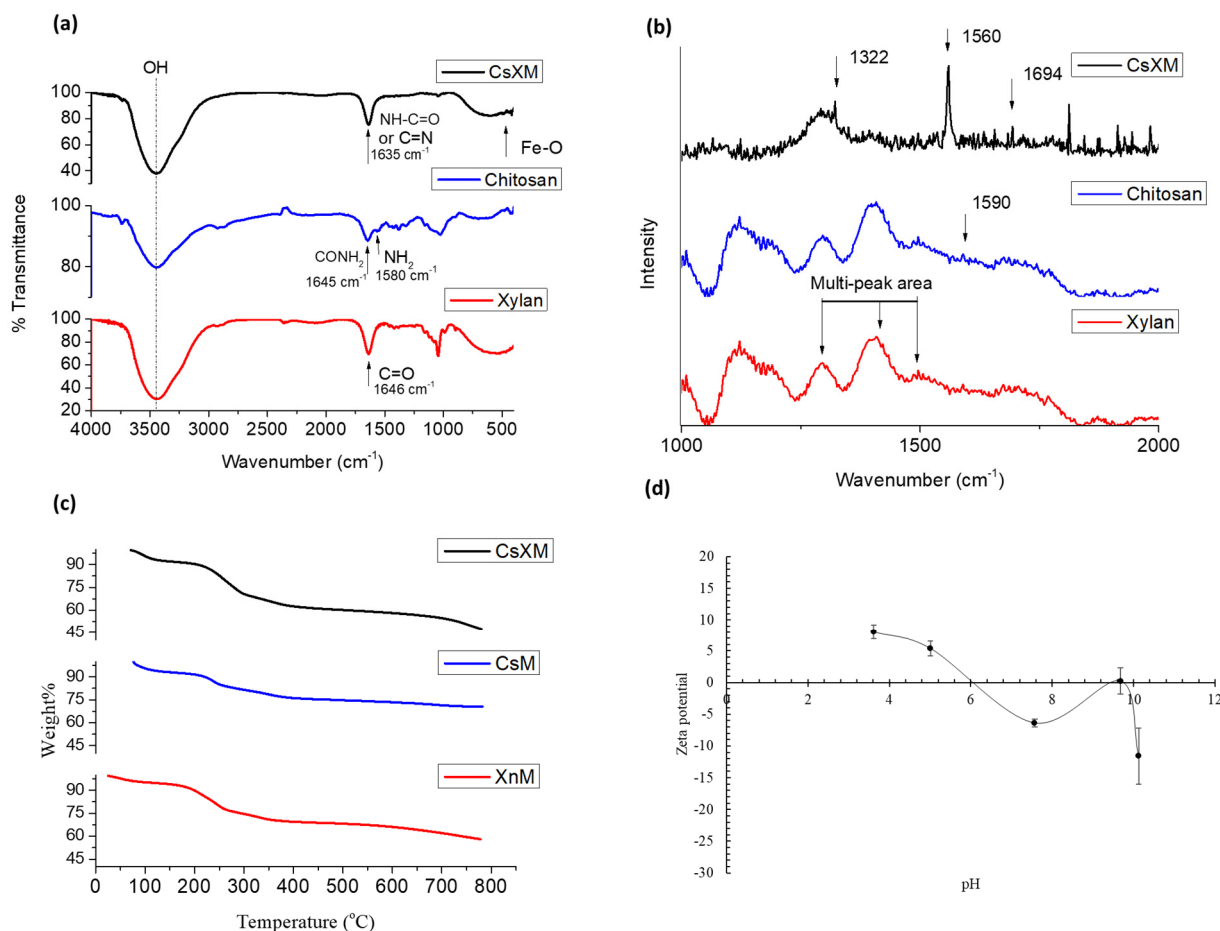


Figure 1. (a) FTIR spectra of CsXM, chitosan and xylan, (b) Raman spectra for CsXM, chitosan, and xylan, (c) TGA profiles for CsXM, CsM, and XnM, and (d) zeta potential of CsXM at different pHs.

To assess the thermal stability of CsXM, the TGA profile for CsXM was compared to those of CsM and XnM. As is clear from Figure 1c, CsXM showed comparable stability to that of CsM and XnM, where only about 5% of the nanocomposites degraded in the range of 100–200 °C, and about 5–7% of its weight was lost below 100 °C due to moisture loss. At 750 °C, the total weight remaining was about 50%, 70%, and 60% for CsXM, CsM, and XnM, respectively. In previous literature, chitosan-coated magnetite showed similar behavior where slight weight reduction occurred before 100 °C, although the total weight remaining at 600 °C was about 65% [58]. The zeta potential of CsXM (Figure 1d) ranged from 8.02 to −11.6 over the employed pH range of 3.6–10.1, which indicates an almost neutral charge over the whole studied range [59].

With regard to the textural properties, Table 1 shows that the BET surface area of CsXM exceeded that of chitosan and xylan by about 12.0 and 37.0 times, respectively; however, it was lower than those of CsM and XnM by 3.6 and 1.9 times, respectively, while its Langmuir surface area was 11.0 and 36.6 times higher than that of chitosan and xylan, respectively, and lower than CsM and XnM by 3.5 and 1.9 times, respectively. The majority of the pore sizes of CsM, XnM, and CsXM lay in the range of 2–50 nm, indicating a mesoporous structure along with some micropores, as confirmed by the type IV BET isotherms and pore size distribution curves in Figures S3 and S4d–f of the SI, respectively. The BET isotherms

of chitosan and xylan, however, followed type II isotherm, which indicates a macroporous (>50 nm) structure (Figures S3 and S4a,b, SI). This explains the fact that CsXM possesses a larger surface area than chitosan and xylan owing to its smaller-sized pores. The surface area trend is also consistent with that of the average particle size calculated from BET measurements (Table S1), where CsXM is larger in size than CsM and XnM but smaller than chitosan and xylan. The BJH pore volume exhibited a similar trend to that of the surface area, with the CsXM pore volume exceeding that of chitosan and xylan by about 50 and 91%, respectively, while subceeding that of CsM and XnM by 87 and 67%, respectively. The table also shows that the BET surface areas and pore volumes of CsXM and chitosan/xylan films were comparable, whereas the Langmuir surface area of the latter was much larger, probably since it possesses more micropores (Figures S3c and S4c, SI).

Table 1. Parameters of BET nitrogen adsorption-desorption isotherms.

	BET Surface Area (m ² /g)	BJH Pore Volume (cm ³ /g)	Langmuir Surface Area (m ² /g)
CsXM	21.81	0.014	32.22
Chitosan	1.82	0.007	2.93
Xylan	0.59	0.001	0.88
Chitosan/xylan	22.78	0.018	177.24
CsM	79.31	0.109	114.27
XnM	41.67	0.043	60.08

The morphology of the CsXM nanoparticles was investigated by both TEM and SEM, as depicted in Figure 2. Since magnetite has a higher electron density than the biopolymer, it clearly appears as dark regions in the TEM image (Figure 2a), which shows a dispersion of spherical to octahedral magnetite nanoparticles with coating of the biopolymers. These images are similar to those reported in previous literature for natural biopolymer-capped magnetite and for dextran-coated iron oxide nanoparticles [60,61]. The diffraction pattern for CsXM in Figure 2b suggests a multi-crystalline structure of magnetite owing to the appearance of multiple rings. As shown in the histogram for particle size distribution (Figure 2c), the mean particle size of magnetite after coating was 11 ± 2.3 nm, compared to 8.1 ± 3.0 nm for bare magnetite (Figure S2b, SI). The SEM micrograph (Figure 2d) shows a rough surface that implies successful coating [62].

3.2. Adsorption Performance

The adsorption behavior of Pb(II), SA, and CR onto CsXM was investigated under different conditions. The working pH for the adsorption of Pb(II), SA, and CR was 5.5 ± 0.1 , 4.0 ± 0.3 , and 6.1 ± 0.2 , respectively. At these pH levels, the almost neutral CsXM is likely to bind to the positively charged Pb (II) by complexation, and to the negatively charged SA (pK_a 2.98) and CR (pK_a 4.1) (www.chemicalbook.com, accessed on 15 September 2022) by hydrogen bonding or physical forces. At pH levels below 5.5, the adsorbent will still exist in the neutral to positive form; however, the H⁺ ions in solution will compete with Pb(II) on the electron-rich groups at the adsorbent surface, thus hindering Pb(II) complexation. Above pH 5.5, Pb(II) will complex with hydroxyl ions or form hydroxide that precipitates, and this will again lead to less adsorption [63]. In the case of SA, pHs lower than 4 will result in a decrease of the negative charge on the drug molecule, and hence, SA species will be predominant in the neutral form as per its speciation diagram (www.chemicalize.com, accessed on 19 January 2023). This will, in turn, decrease the interaction between SA and the adsorbent. The same effect is anticipated at pH > 4, where electrostatic repulsion will take place between the slightly negative adsorbent and the predominant negative SA species (www.chemicalize.com, accessed on 19 January 2023). Regarding CR, pHs below 6 might slightly increase the removal efficiency since the CR will almost remain negatively charged (www.chemicalize.com, accessed on 19 January 2023), while the adsorbent will be neutral to positively charged. On the other hand, increasing the

pH above 6 might reduce the removal due to electrostatic repulsion between the slightly negative adsorbent and the negative CR. Since the amide complexes are considered to be relatively strong bases, they can bind to Pb(II) via Lewis acid-base interactions, and can possibly be involved in acid-base interactions with SA or CR [64]. Table 2 shows the percent removal of the studied contaminants by CsXM, CsM, and XnM at an initial concentration of 50 ppm, adsorbent dose of 0.67 g/L, and temperature of 25 ± 2 °C. Clearly, CsXM shows a comparable removal for SA relative to CsM and a higher removal relative to XnM, albeit lower removal for Pb(II) relative to XnM, which could be attributed to the less available glucuronic acid groups of xylan in CsXM as compared to XnM. These groups are negatively charged under the working pH (the pK_a of glucuronic acid is 3.21) and thus can interact electrostatically with Pb(II); however, they can repel the negatively charged SA. Nonetheless, CsXM removed slightly more Pb(II) than CsM, possibly due to the formation of a stable amide-Pb(II) complex in the case of CsXM, through the interaction of Pb(II) with either the nitrogen atom or carbonyl oxygen atom of the amide. The binding of Pb(II) to CsM can, however, occur only through the N atom of the amine group. In the case of CR, CsM gave the highest removal efficiency; however, the removal was slightly higher than that of XnM or CsXM. Therefore, CsXM can potentially remove positively charged and negatively charged contaminants by forming stable bonds with them. The chitosan/xylan composites have been reported in the literature to have high chemical and mechanical stabilities [48,65]. Therefore to improve the removal efficiency of CsXM, further investigations were conducted under different operating conditions.

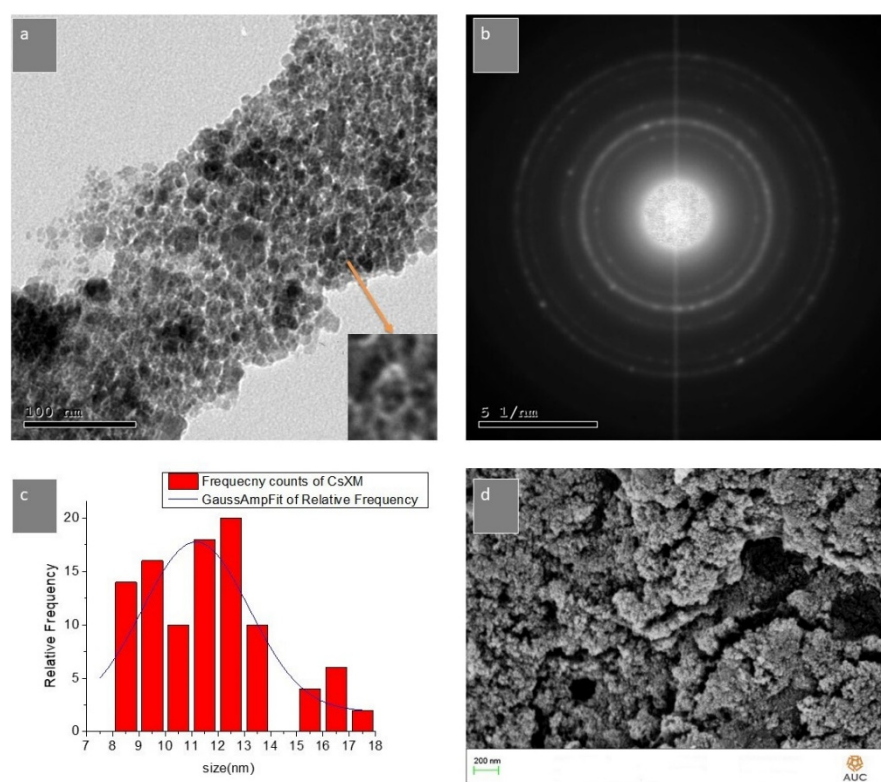


Figure 2. (a) TEM image, (b) Diffraction pattern, (c) particle size distribution histogram, and (d) SEM of CsXM nanoparticles.

A kinetic adsorption study was conducted at 50 ppm of each contaminant using 0.67 g/L of CsXM. As shown in Figure S5a of SI, the normalized kinetic profiles for the adsorption of Pb(II), SA, and CR approached their equilibrium in the order of CR (30 min) > SA (2 h) > Pb(II) (3 h), where they reached a plateau. By fitting the profiles to the pseudo-first and pseudo-second order models (Equations (S3) and (S4) of SI), it can be deduced that the latter represented a better fit, as is evident from its higher R^2 values

presented in Table 3. Hence, adsorption occurred via different mechanisms, including surface reaction, film diffusion, and intra-particle diffusion. By inspecting the values of k_2 for the adsorption of Pb(II), SA, and CR given in Table 3, it is clear that CR adsorption possesses the highest k_2 value, implying the highest adsorption rate, followed by SA then Pb(II) adsorption. This trend is in accordance with the equilibrium time pertaining to the adsorption of each contaminant. The q_e values predicted by the pseudo-second order model were in good agreement with the experimental values for Pb(II), SA, and CR. To elucidate the underlying adsorption mechanism, the adsorption profiles were fitted to the Weber and Morris intra-particle diffusion model (Equation (S5) of SI), the linear plots of which are shown in Figure S5e of SI, while its predicted parameters are given in Table 3. For Pb(II), the line passes through the origin, indicating that pore diffusion is the rate-limiting step. This behavior was unlike that for SA and CR, whose plots were bi-linear, with the first stage passing through the origin in the case of SA, implying negligible boundary layer limitations, while it did not pass through the origin in the case of CR, indicating that its adsorption is controlled by film diffusion [66]. As is presented in Table 3, the intra-particle diffusion rate constant (k_{id}) for SA adsorption was lower than that of Pb(II), indicating a faster intra-particle diffusion rate for the latter. This could be ascribed to the smaller size of Pb(II), ~0.4 nm hydrated sphere, which allows for more accessibility to the pores and hence faster pore diffusion than SA. On the other hand, the k_2 value for SA was greater than that of Pb(II), indicating a faster rate for the overall adsorption process, albeit with lower k_{id} compared to Pb(II). This behavior could be attributed to the fact that SA approaches equilibrium by saturating the adsorption sites faster than Pb(II), as is clear from their kinetic profiles (Figure S5a). SA binds to CsXM by physical interactions, which are faster than the chemical interactions that are likely to occur between Pb(II) and the amide bond or possibly the Schiff base. However, it is possible that the chemisorption of Pb(II) was preceded by physisorption where Pb(II) approached the surface of CsXM via weak physical forces, and subsequent chemisorption then took place as the Pb(II) got closer to the surface. In this case, no activation energy was required and the process initially involved fast kinetics. This hypothesis was supported by calculating the initial rates of adsorption, v_i (Equation (S6) of SI) based on the q_e and k_2 values from the pseudo-second order kinetic model. By inspecting these rates (Table 3), it was inferred that Pb(II) was initially adsorbed faster than SA, which was only justified when Pb(II) was adsorbed physically. Thus, it adsorbed faster by virtue of its size, which entailed high charge density. Regarding CR, its adsorption showed the highest k_{id} , and thus the fastest intra-particle diffusion rate, possibly because its adsorption was governed by film diffusion owing to its larger particle size (1–2.53 nm) that limited its accessibility to micropores (<2 nm) or smaller mesopores. The negative value of the film diffusion coefficient (C) indicated that the boundary layer formed on the surface of CsXM hindered the intra-particle diffusion process of CR [67]. The CR initial rate was the least among the three contaminants owing to the film diffusion limitations; this was followed by SA then Pb(II), for the same reasons indicated earlier.

Table 2. Percent removal of Pb(II), SA, and CR by CsM, XnM, and CsXM. Chemical structures of SA and CR are given in the table.

	Pb(II)	SA	CR
CsM	22.9 ± 0.1	16.5 ± 0.0	17.6 ± 0.1
XnM	49.5 ± 0.1	3.9 ± 0.0	11.1 ± 0.2
CsXM	28.9 ± 2.3	18.1 ± 3.1	9.8 ± 1.3

Table 3. Kinetic parameters for the adsorption of Pb(II), SA, and CR on CsXM.

	Pseudo-First Order			Pseudo-Second Order			Intra-Particle Diffusion			
	q_e mg/g	k_1 min^{-1}	R^2	q_e mg/g	k_2 $\text{G}\cdot\text{mg}^{-1}\cdot\text{min}^{-1}$	R^2	v_i min^{-1}	C	k_{id} $\text{mg}\cdot\text{g}^{-1}\cdot\text{min}^{-0.5}$	R^2
Pb(II)	22.26	0.014	0.9916	29.06	0.0007	0.9982	9.272	0	1.630	0.9923
SA	5.50	0.009	0.6971	13.49	0.0026	0.9920	3.037	0	1.107	0.9895
CR	0.82	0.004	0.08	8.10	0.0220	0.9948	1.445	-6.624	2.665	0.9519

The equilibrium adsorption capacity and percent removal of the three tested contaminants were determined for different initial concentrations of each contaminant using 0.67 g/L of CsXM at 25 ± 2 °C and a working pH of 5.5 ± 0.1 , 4.0 ± 0.3 , and 6.1 ± 0.2 , for Pb(II), SA, and CR, respectively (Figure 3). For Pb(II), the percent removal averaged around 27.8 ± 1.98 over the studied initial concentration range (10–50 ppm), while q_e increased linearly with increasing the initial concentration reaching about 21.68 mg/g at 50 ppm, probably due to the increase in the mass transfer driving force as a result of the larger concentration gradient [68]. This behavior has also been observed in previous work conducted at almost the same initial Pb(II) concentration range of 5–50 ppm, and at an adsorbent dose of 0.2 g/L and temperature of 25 °C, using AC/HKUST-1 nanocomposite as an adsorbent [69]. For SA adsorption capacity, a similar behavior to that of Pb(II) was encountered; however, q_e reached 12.82 mg/g. As for the removal of SA, it averaged around 16.83 ± 2.41 over the studied initial concentration range of 10–50 ppm. CR, on the other hand, showed an opposite trend in its removal percent to that of SA, as it decreased to almost half from about 44% to 21% when the concentration was doubled from 10 to 20 ppm. Similar finding was reported for the adsorption of CR onto *Antigonon leptopus* leaf powder where the percent removal of CR decreased upon increasing the initial concentration [70]. Above 20 ppm, the removal maintained an average constant value of about $15.56 \pm 4.9\%$. Regarding the adsorption capacity, this increased slightly with increasing concentration until it reached 8.05 mg/g at 30 ppm, then it remained almost constant over the range of 30–50 ppm. This behavior, which varied from that of SA and Pb(II), was likely due to the different underlying adsorption mechanisms of CR being controlled by film diffusion, while the adsorption of SA and Pb(II) was controlled by pore diffusion.

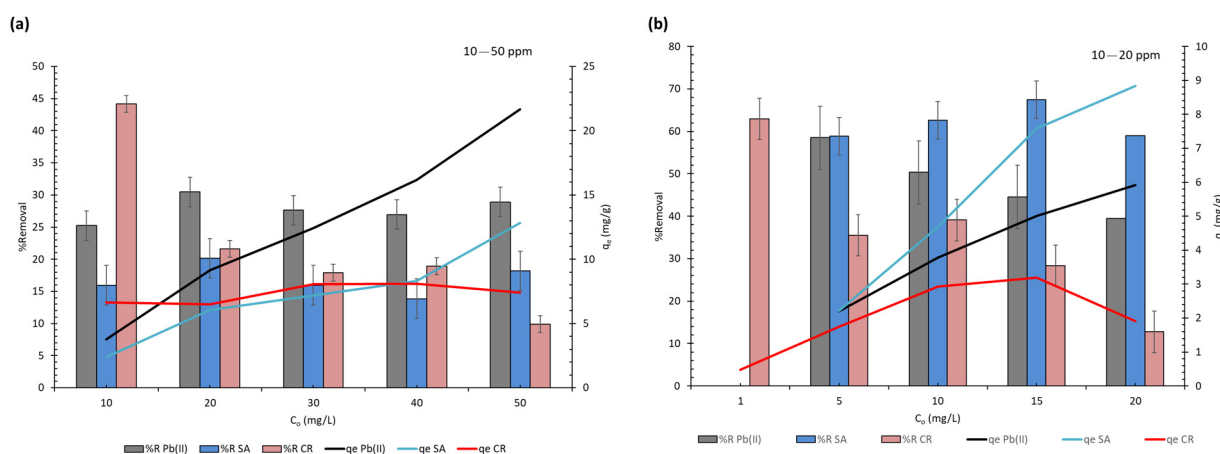


Figure 3. Effect of initial concentration on q_e and %removal for the three tested contaminants at 25 ± 2 °C using (a) 0.67 g/L of CsXM in the range of 10–50 ppm, and (b) 1.33 g/L of CsXM in the range of 1–20 ppm. Adsorption was conducted at 5.5 ± 0.1 , 4.0 ± 0.3 , and 6.1 ± 0.2 , for Pb(II), SA, and CR, respectively. Error bars are expressed as mean value \pm SD ($n = 3$).

When the adsorption of the contaminants was investigated at the lower initial concentration range of 1–20 ppm to be more relevant to surface water, the removal efficiencies appreciably

increased for SA, Pb(II), and CR, reaching about 70%, 60%, and 60% at 15, 5, and 1 ppm, respectively. However, the removal of Pb(II) and SA below 5 ppm could not be determined since the removal was high, and hence, the remaining concentration in the solution was below the limit of detection.

To describe the adsorption behavior of the three contaminants on CsXM under equilibrium conditions, the adsorption isotherms shown in Figure 4 were fitted to Langmuir and Freundlich models (Equations (S7) and (S8) in SI); the isotherm parameters are compiled in Table 4. As confirmed from its higher R^2 values (Table 4), the Freundlich model described the adsorption isotherms of Pb(II), SA, and CR better than the Langmuir model, and hence implied multi-layer adsorption on a heterogenous surface with non-energetically equivalent sites. Root mean square error (RMSE) values also confirmed that Freundlich was a better fit since Freundlich showed lower values than the Langmuir model. The value for $1/n$ (Table 4) was slightly greater than 1 in the case of Pb(II), indicating a linear to unfavorable adsorption [71], while it was less than 1 in the case of SA and CR, implying favorable adsorption [72].

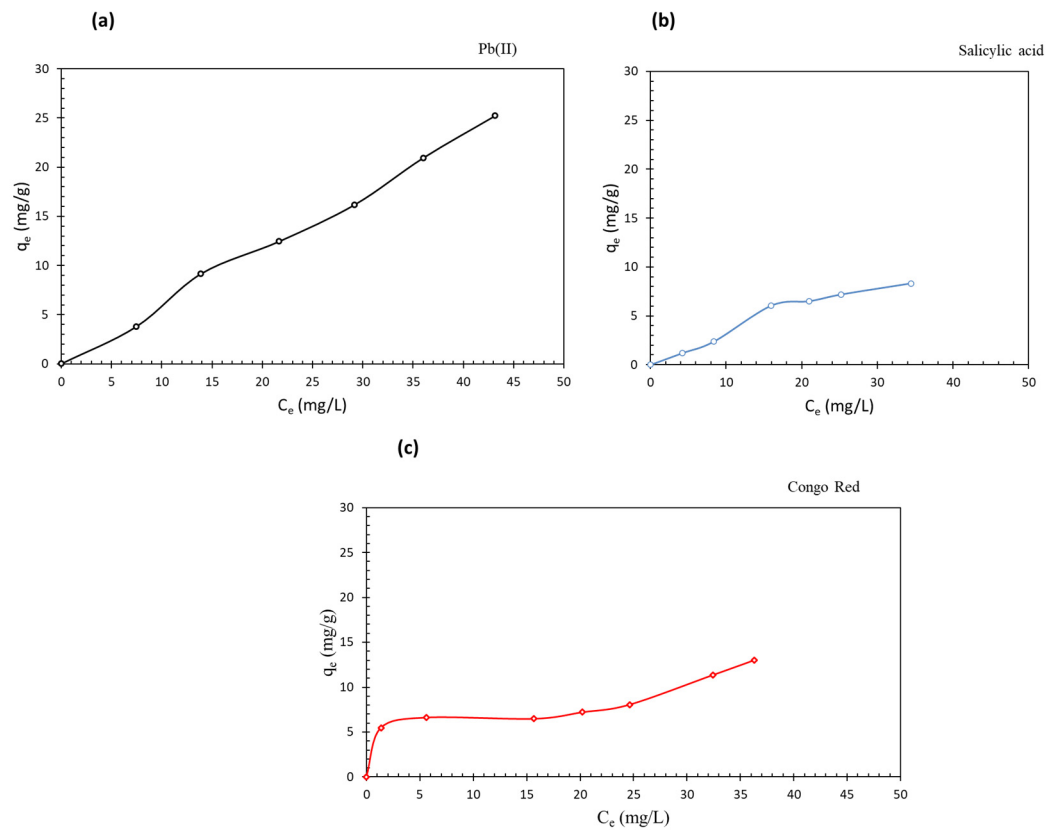


Figure 4. Adsorption isotherms for the three studied contaminants at 25 ± 2 °C and pHs of 5.5 ± 0.1 , 4.0 ± 0.3 , and 6.1 ± 0.2 for (a) Pb(II), (b) SA, and (c) CR, respectively.

Table 4. Isotherm parameters as predicted by Langmuir and Freundlich models.

	Langmuir Isotherm				Freundlich Isotherm			
	q_m mg/g	K_d	R^2	RMSE	K_f (mg/g) (L/mg) ⁿ	$1/n$	R^2	RMSE
Pb(II)	434.78	784.56	0.0433	0.131	0.51	1.04	0.9859	0.074
SA	4.31	13.06	0.3681	0.400	0.35	0.92	0.9649	0.133
CR	13.23	8.91	0.7676	0.673	1.32	0.60	0.9833	0.443

Increasing the adsorbent dose could enhance adsorption by providing more active sites. However, in some cases, and particularly for industrial applications, there might be a need to decrease the adsorbent dose applied per each adsorption run to overcome the problem of adsorbent agglomeration at high doses and minimize the mass transfer effects arising from large-scale application. Thus, the dose was either divided into two consecutive adsorption cycles run in the same tank, or alternatively, it was split into two tanks that were run simultaneously to reduce the operation time. As shown in Figure 5, increasing the dose applied in one cycle provided removal efficiencies that reached 62.46, 52.09, and 45.15%, and 65.95, 62.90, and 70.35% in Pb(II), SA, and CR, respectively at a dose of 3 and 6 g/L, compared to higher removal efficiencies of 75.68, 58.54, and 51.48%, and 77.43, 73.22, and 71.17% obtained for the same contaminants, respectively, when dividing these doses into two consecutive adsorption cycles (see figure insets). At 2 g/L, respective removal efficiencies of 55.34, 43.09, and 32.07% for Pb(II), SA, and CR were achieved when the dose was applied in one cycle, which was comparable to 56.68, 44.72, and 35.04%, respectively, obtained when the dose was divided upon two cycles.

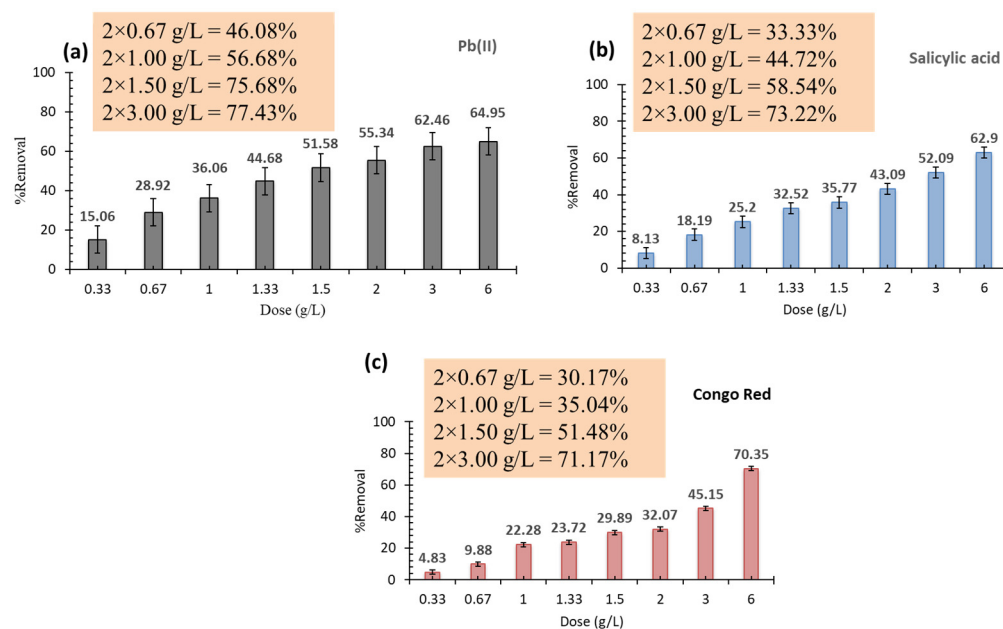


Figure 5. Bar graph of the dose effect of CsXM applied in one cycle of adsorption for (a) Pb(II), (b) SA, and (c) CR, while results for the 2 consecutive cycles of adsorption are embedded in the Figure insets. The initial concentration was 50 ppm, the contact time was 4 h, the temperature was 25 ± 2 °C, and pH values were 5.5 ± 0.1 , 4.0 ± 0.3 , and 6.1 ± 0.2 , for Pb(II), SA, and CR, respectively. Error bars are expressed as mean value \pm SD ($n = 3$).

3.3. Adsorption in Ternary System

Figure 6 compares the percent removal of the three tested contaminants in single and ternary systems at pH 5.5 and 4.0. At both pHs, the removal of CR decreased in the ternary system relative to the single one due to the competition of Pb(II) and SA over the active sites. The adsorption of CR was controlled by film diffusion limitations due to the larger size of CR compared to Pb(II) and SA, and this hindered its accessibility to the pores. At pH 5.5, Pb(II) showed higher removal than SA in single systems and could therefore be more competitive than SA in ternary systems; i.e., it occupied more active sites. The adsorption of Pb(II) in the ternary system was unaffected by the presence of SA and CR, and hence, Pb(II) maintained the same removal as in single systems. The removal of SA, however, slightly increased in ternary systems, probably as a result of complexation with the bound Pb(II). In contrast, at pH 4.0, SA showed higher removal efficiency than Pb(II) in single systems, and hence, it is likely that it becomes more competitive than Pb(II) in

ternary systems. Thus, Pb(II) was anticipated, this time, to chelate with the already bound SA. The possibility of chelation/complexation between Pb(II) and SA has been evidenced in previous literature [73]. It was also observed that the removal efficiency of Pb(II) at pH 4.0 was less than its removal at pH 5.5 due to the competition of protons over the active sites, which reduced the adsorption of Pb(II) in the more acidic medium. The removal of SA at pH 5.5, on the other hand, was less than its removal at pH 4.0, possibly as a result of the competition of the hydroxyl ions in the solution over the active sites.

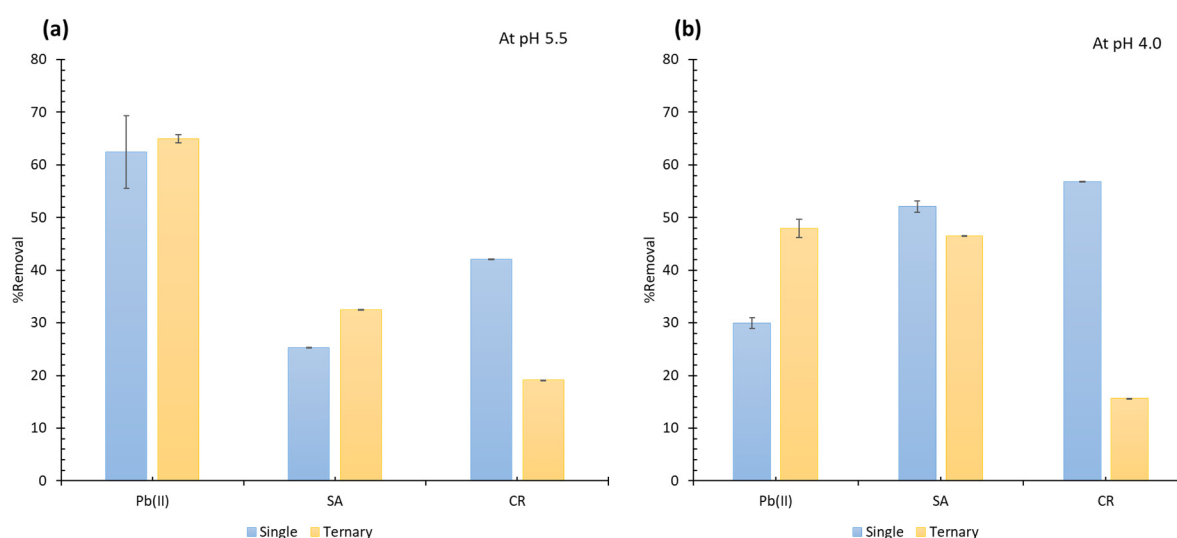


Figure 6. Adsorption of the tested contaminants in single and ternary systems at pH 5.5 (a) and 4.0 (b) using a 3 g/L adsorbent dose and an initial concentration of 50 ppm at 25 ± 2 °C. Error bars are expressed as mean value \pm SD ($n = 3$).

The selectivity coefficients α_B^A (Table 5) for Pb(II)/SA, Pb(II)/CR, and SA/CR were calculated (Equation (S9) of SI [74]) to compare the competitiveness of the contaminants in the ternary system. By comparing the values of the coefficients in the table, it was inferred that Pb(II) adsorption was more favorable than SA and CR, while SA adsorption was more favorable than CR at pH 5.5, and this was in agreement with the removal efficiencies presented in Figure 6. On the other hand, at pH 4.0, Pb (II) was almost equally competitive to SA; however, it was more competitive than CR. Additionally, SA was more competitive than CR, which was also in accordance with the removal efficiencies given in Figure 6.

Table 5. Selectivity coefficients of the tested contaminants in the ternary system.

A/B	α_B^A	
	pH 5.5	pH 4.0
Pb(II)/SA	3.85	1.06
Pb(II)/CR	7.83	4.96
SA/CR	2.03	4.70

To conceive a removal strategy for ternary systems, a two-step adsorption separation process was proposed. Adsorption was conducted first at pH 5.5, where Pb(II) was mainly removed (~60%), with some SA (~30%) and minimal CR (~20%). The effluent solution from this step, which constituted primarily CR (~80%) and SA (~70%) with some Pb(II) (~40%), was then fed to a second stage at pH 4.0. Since CR was the least competitive and SA was probably more competitive than Pb (II) at pH 4.0, despite having $\alpha_B^A \sim 1$, by virtue of its much larger amount, it was anticipated that SA would be the most competitive and therefore would be mostly removed in this step. SA would thus occupy more active sites than Pb(II), which is expected to exist in a much lower amount than SA; nevertheless, Pb(II)

would still be highly removed since it would chelate with the bound SA. The effluent from the second stage would be composed primarily of CR, and hence, could be separated as a single system in a separate step.

3.4. Adsorption Mechanism

To elucidate the adsorption mechanism, FTIR measurements were performed before and after the adsorption of Pb(II), SA, and CR, as depicted in Figure S7 of SI. Clearly, the intensity of the OH peak changed significantly when CsXM was bound to Pb(II), SA, and CR, indicating that possible physical interactions, such as hydrogen bonding, dipole-dipole between the contaminants and the almost neutral CsXM, could have occurred. Also, a slight shift in the amide bond or Schiff base peak appeared as reported in the literature [75], upon the binding of CsXM to each of Pb(II), SA, and CR. This suggests that Pb(II) binds to CsXM by mainly chelation/complexation with possibly some physical interactions, while SA and CR bind to CsXM via primarily electrostatic interaction and hydrogen bonding [76,77]. Some of the possible interactions are illustrated in Figure 7. According to previous literature, chitosan/EDTA-coated magnetite was efficient in adsorbing Pb(II) from aqueous solutions via amide bond interaction, while it was reported that hyaluronic acid methacrylate hydrogel adsorbed Pb(II) through complexation to either the amine or carbonyl group of the amide bond [78,79]. In addition, salen-functionalized graphene oxide was successful in the adsorption of Pb(II) from contaminated water via coordinate complexation with the adsorbent Schiff base [80], and SA and CR were successfully bound to pine wood biochar and Schiff base–chitosan grafted l-monoguluronic acid, respectively, by hydrogen bonding [81,82].

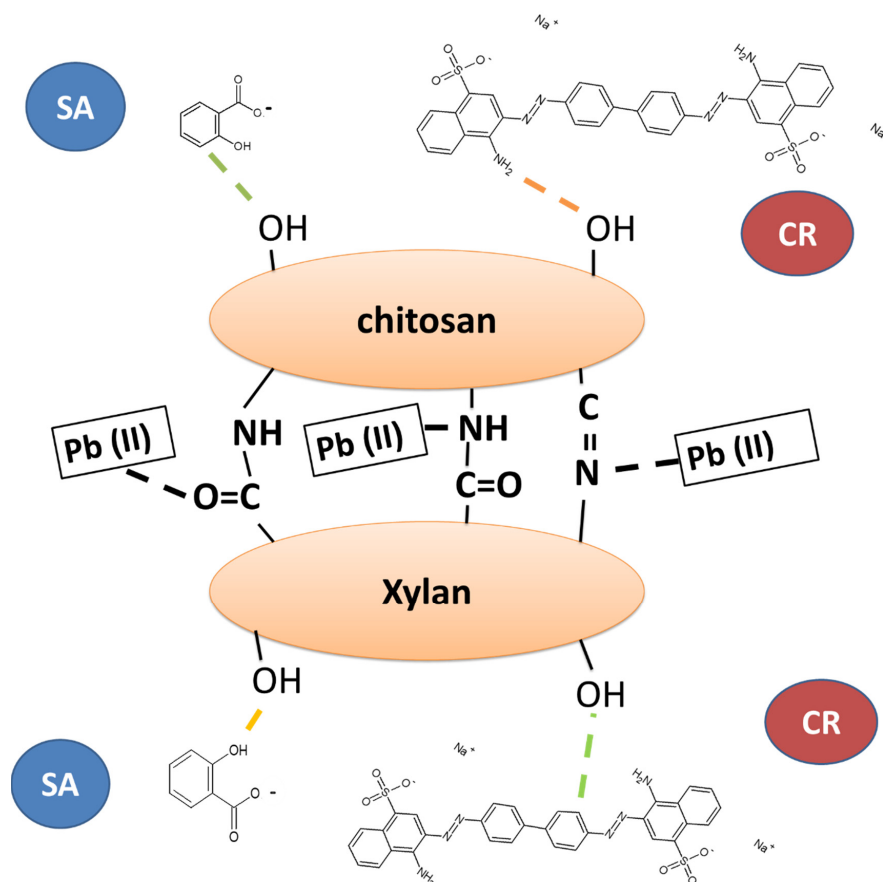


Figure 7. Some possible mechanisms of interaction for the adsorption of Pb(II), SA, and CR on CsXM, with black dotted line for chelation, orange dotted line for H-bonding, and green dotted line for van der Waals forces.

3.5. Regeneration

In this study, Pb(II), SA, and CR were adsorbed using either 0.67 or 1.33 g/L of CsXM at 25 °C ± 2, and pH of 5.5 ± 0.1, 4.0 ± 0.3, and 6.1 ± 0.2, for Pb(II), SA, and CR, respectively, and 50 ppm of each contaminant; they were then regenerated using 0.1 N HCl in the case of Pb(II) adsorption and 0.1 N NaOH in the case of SA and CR adsorption. The adsorption-desorption process was repeated for three consecutive cycles. As shown in Figure 8a, the percent removal of Pb(II), SA, and CR remained almost constant over the three regeneration cycles when 0.67 g/L of CsXM was applied. Increasing the dose from 0.67 g/L to 1.33 g/L (Figure 8b) gave a different regeneration behavior for SA and CR, where the percent removal decreased to about more than half the original value after the first cycle; however, Pb(II) removal efficiency decreased by about 6% only. This could be owing to the high desorbing power of HCl when used as a regenerant for Pb(II) relative to the weak desorbing agent of SA and CR. Besides, SA and CR were more favorably adsorbed onto CsXM than Pb(II), as confirmed by their Freundlich constant ($1/n$), and hence, were more difficult to desorb. Hence, there might be a need to apply larger amounts of the desorbing agent for SA and CR when higher doses of CsXM are applied. It is, thus, evident that the desorbing agents can be successful in maintaining the adsorption power of CsXM. Although the regeneration in the case of Pb(II) adsorption was efficient, no more cycles could be performed since the adsorbent became finer in size and more difficult to collect by magnetic decantation since its zeta potential changed after regeneration, indicating possible deterioration of the composite material. However, it should still be safe to discard the adsorbent given the biodegradable and environmentally friendly nature of its materials. Before discarding the adsorbent, it is also possible to soak it in the regenerant for sufficient time to allow for the degradation of the polymeric materials, thus leaving out the magnetite nanoparticles to be collected by a magnet.

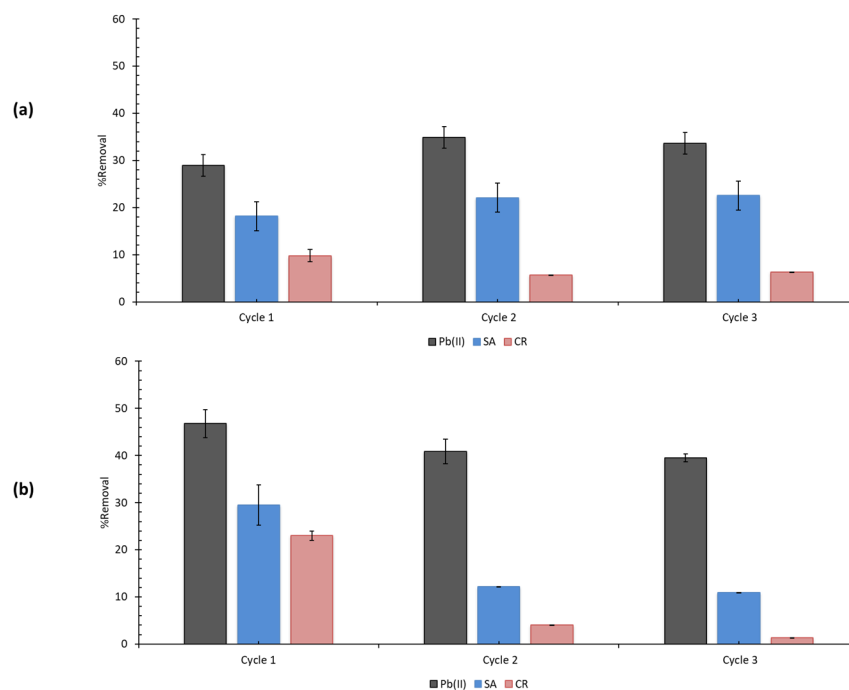


Figure 8. Regeneration of CsXM after adsorption of Pb (II), SA, and CR using 0.1 N HCl for the former and 0.1 N NaOH for the latter two at doses of 0.67 g/L (a) and 1.33 g/L (b). Error bars are expressed as mean value ±SD.

4. Comparison with Literature

The adsorption capacities of CsXM were compared to other relevant bio-based adsorbents previously reported in the literature (Table 6). It can be inferred that CsXM removed

Pb(II) at a comparable adsorption capacity to those of other reported biopolymer-based adsorbents [83,84]. The adsorption of SA onto CsXM was also comparable to the adsorption of acetyl-SA on chitosan/waste coffee grounds composite [85]. However, it was less than that of molecularly imprinted polymers (MIPs), which is understandable given the sophistication and high cost involved in synthesizing MIPs [86]. CsXM also adsorbed CR at a comparable adsorption capacity to that shown for orange peels [87]; however, it had less adsorption capacity than that of chitosan/clay composites, probably due to the high surface area provided by the clay, which also might suffer from other advantages in its handling and limited applicability to negatively charged contaminants since the positively charged groups on the adsorbent played a main role in adsorption [27].

Table 6. Comparison of CsXM adsorption capacities with those of other bio-based adsorbents previously reported in the literature.

Adsorbent	Adsorbate	q_m (mg/g)	Ref.
Carboxymethyl starch-coated manganese ferrite	Pb(II)	34.15 (Freundlich)	[83]
Hydroxysodalite-chitosan composites	Pb(II)	17.85 (Langmuir)	[84]
Crosslinked acrylamide grafted chitosan-based mimic SA and cadmium dual imprinted polymer	SA	40.80 (Langmuir)	[86]
Chitosan/waste coffee grounds composite	Acetyl-SA	9.97 (Freundlich)	[85]
Chitosan/montmorillonite	CR	54.52 (Langmuir)	[27]
Orange peel	CR	14.00 (Langmuir)	[87]
CsXM	Pb(II)	25.20 (Freundlich)	This study
	SA	11.34 (Freundlich)	
	CR	13.01 (Freundlich)	

5. Conclusions

Thermally stable mesoporous chitosan/xylan-coated magnetite (CsXM) nanoparticles of 11 ± 2.3 nm were successfully prepared. FTIR measurements confirmed the formation of a superimposed peak of the amide group and possibly the Schiff base between chitosan and xylan. CsXM was efficient in binding SA and CR mostly by electrostatic interactions and hydrogen bonding, and Pb(II) ions via chelation. By increasing the dose of CsXM to 6 g/L, removal efficiencies of 64.95, 62.9, and 70.35% were obtained for 50 ppm of Pb(II), SA, and CR at $25 \text{ }^\circ\text{C} \pm 2$, and pH of 5.5 ± 0.1 , 4.0 ± 0.3 , and 6.1 ± 0.2 , respectively. Dividing the higher doses into two adsorption cycles proved efficient for increasing the percent removal since it mitigated the mass transfer problems arising from adsorbent agglomeration. The two cycles could be run consecutively in one tank or simultaneously in two tanks to reduce the operational time. This demonstrates the potential of applying this approach for large-scale industrial applications.

Investigating the removal efficiencies of CsXM at a lower concentration range of 1–20 ppm for the three contaminants showed that it can be efficiently utilized for surface water and is applicable for industrial wastewater. In addition, CsXM can be easily separated from water by a magnetic field, which makes it practical to use. It also provides high removal efficiencies while utilizing fewer amounts of chitosan and xylan in its synthesis when compared to the similar chitosan/xylan composites reported in previous literature [32,34].

Adsorption kinetics followed the pseudo-second order model, with CR showing the fastest rate followed by Pb(II), then SA. The adsorption of CR was controlled by film diffusion, while the adsorption of Pb(II) and SA was governed by pore diffusion, which led to their slower kinetics relative to CR. Adsorption behavior could be best described by the Freundlich isotherm, indicating multi-layer adsorption. Adsorption in ternary systems proved successful in the removal of Pb(II) and SA while almost maintaining their

removal efficiency as in single systems, however it decreased significantly in the case of CR. CsXM could be regenerated efficiently for three cycles using HCl after Pb(II) adsorption; however, regeneration with NaOH after SA and CR adsorption was not efficient. Hence it is recommended to discard the adsorbent since it is composed of environmentally safe biodegradable materials that can potentially be obtained from natural resources or waste materials.

Supplementary Materials: The following supporting information can be downloaded at: <https://www.mdpi.com/article/10.3390/w15040829/s1>; Figure S1: NMR chart for beechwood xylan showing the presence of acetyl groups at 2.2 ppm; Figure S2: TEM image of bare magnetite (a), its particle size histogram (b), and the XRD profiles for bare magnetite (c) and CsXM (d); Figure S3: BET isotherms for chitosan (a), xylan (b), chitosan/xylan (c), CsXM (d), CsM (e), and XnM (f); Figure S4: Pore volume distribution for chitosan (a), xylan (b), chitosan/xylan (c), CsXM (d), CsM (e), and XnM (f); Figure S5: Normalized kinetic plots for the effect of contact time (a), pseudo-second order linear fits for the adsorption of Pb(II) (b), SA (c), and CR (d), and (e) intra-particle diffusion fits for the adsorption of Pb(II), SA, and CR. Initial concentration of tested contaminants was 50 ppm, adsorbent dose was 0.67 g/L at $25\text{ }^{\circ}\text{C} \pm 2$, with pH of 5.5 ± 0.1 , 4.0 ± 0.3 , and 6.1 ± 0.2 , for Pb (II), SA, and CR, respectively, and at room temperature; Figure S6: UV/VIS spectra for the ternary system comprising Pb(II), SA, and CR before adsorption at pH 5.5 (upper panel) and pH 4.0 (lower panel); Figure S7: FTIR peaks for CsXM before and after adsorption of Pb(II), SA, and CR; Table S1: XRD 2θ values for both magnetite and CsXM; Table S2: BET measurements of particle size.

Author Contributions: Performing all experiments and writing the original draft, H.H.F.; Supervision and revision, M.N.; Supervision, writing, revision and editing, M.M.H.E.-S. All authors have read and agreed to the published version of the manuscript.

Funding: This work was supported by the American University in Cairo through a Ph.D. research grant for purchasing chemicals and consumables, and by USAID ASHA Grant Number: AID-ASHA-G-17-00010 for capacity building, which provided the lab instruments.

Data Availability Statement: Not applicable.

Conflicts of Interest: The authors declare no competing interests.

References

1. Rout, P.R.; Zhang, T.C.; Bhunia, P.; Surampalli, R.Y. Treatment technologies for emerging contaminants in wastewater treatment plants: A review. *Sci. Total Environ.* **2021**, *753*, 141990. [[CrossRef](#)]
2. Michaels, R.A. Legacy contaminants of emerging concern: Lead (Pb), flint (MI), and human health. *Environ. Claims J.* **2020**, *32*, 6–45. [[CrossRef](#)]
3. Kumar, A.; MMS, C.-P.; Chaturvedi, A.K.; Shabnam, A.A.; Subrahmanyam, G.; Mondal, R.; Gupta, D.K.; Malyan, S.K.; Kumar, S.S.; A Khan, S. Lead toxicity: Health hazards, influence on food chain, and sustainable remediation approaches. *Int. J. Environ. Res. Public Health* **2020**, *17*, 2179. [[CrossRef](#)] [[PubMed](#)]
4. Long, Y.; Lei, D.; Ni, J.; Ren, Z.; Chen, C.; Xu, H. Packed bed column studies on lead (II) removal from industrial wastewater by modified *Agaricus bisporus*. *Bioresour. Technol.* **2014**, *152*, 457–463. [[CrossRef](#)]
5. Bahadir, T.; Bakan, G.; Altas, L.; Buyukgungor, H. The investigation of lead removal by biosorption: An application at storage battery industry wastewaters. *Enzym. Microb. Technol.* **2007**, *41*, 98–102. [[CrossRef](#)]
6. Nosek, K.; Styszko, K.; Golas, J. Combined method of solid-phase extraction and GC-MS for determination of acidic, neutral, and basic emerging contaminants in wastewater (Poland). *Int. J. Environ. Anal. Chem.* **2014**, *94*, 961–974. [[CrossRef](#)]
7. Silva, M.; Baltrus, J.; Williams, C.; Knopf, A.; Zhang, L.; Baltrusaitis, J. Mesoporous Fe-doped MgO nanoparticles as a heterogeneous photo-Fenton-like catalyst for degradation of salicylic acid in wastewater. *J. Environ. Chem. Eng.* **2021**, *9*, 105589. [[CrossRef](#)]
8. Smiljanić, D.; Daković, A.; Obradović, M.; Ožegović, M.; Izzo, F.; Germinario, C.; de Gennaro, B. Application of Surfactant Modified Natural Zeolites for the Removal of Salicylic Acid—A Contaminant of Emerging Concern. *Materials* **2021**, *14*, 7728. [[CrossRef](#)]
9. Rawat, D.; Mishra, V.; Sharma, R.S. Detoxification of azo dyes in the context of environmental processes. *Chemosphere* **2016**, *155*, 591–605. [[CrossRef](#)]
10. Wekoye, J.N.; Wanyonyi, W.C.; Wangila, P.T.; Tonui, M.K. Kinetic and equilibrium studies of Congo red dye adsorption on cabbage waste powder. *Environ. Chem. Ecotoxicol.* **2020**, *2*, 24–31. [[CrossRef](#)]

11. Solís, M.; Solís, A.; Pérez, H.I.; Manjarrez, N.; Flores, M. Microbial decolouration of azo dyes: A review. *Process Biochem.* **2012**, *47*, 1723–1748. [[CrossRef](#)]
12. Toor, M.; Jin, B.; Dai, S.; Vimonses, V. Activating natural bentonite as a cost-effective adsorbent for removal of Congo-red in wastewater. *J. Ind. Eng. Chem.* **2015**, *21*, 653–661. [[CrossRef](#)]
13. Gnanamoorthy, G.; Ali, D.; Yadav, V.K.; Dhinakaran, G.; Venkatachalam, K.; Narayanan, V. New construction of Fe₃O₄/rGO/ZnSnO₃ nanocomposites enhanced photoelectro chemical properties. *Opt. Mater.* **2020**, *109*, 110353. [[CrossRef](#)]
14. Gharbani, P.; Tabatabaie, S.; Mehrizad, A. Removal of Congo red from textile wastewater by ozonation. *Int. J. Environ. Sci. Technol.* **2008**, *5*, 495–500. [[CrossRef](#)]
15. Castro-Riquelme, C.L.; López-Maldonado, E.A.; Ochoa-Terán, A.; Alcántar-Zavala, E.; Trujillo-Navarrete, B.; Pérez-Sicairos, S.; Miranda-Soto, V.; Zizumbo-López, A. Chitosan-carbamoylcarboxylic acid grafted polymers for removal of metal ions in wastewater. *Chem. Eng. J.* **2023**, *456*, 141034. [[CrossRef](#)]
16. Prieto-Rodríguez, L.; Miralles-Cuevas, S.; Oller, I.; Agüera, A.; Puma, G.L.; Malato, S. Treatment of emerging contaminants in wastewater treatment plants (WWTP) effluents by solar photocatalysis using low TiO₂ concentrations. *J. Hazard. Mater.* **2012**, *211*, 131–137. [[CrossRef](#)]
17. Demirbas, A. Heavy metal adsorption onto agro-based waste materials: A review. *J. Hazard. Mater.* **2008**, *157*, 220–229. [[CrossRef](#)]
18. Rong, N.; Chen, C.; Ouyang, K.; Zhang, K.; Wang, X.; Xu, Z. Adsorption characteristics of directional cellulose nanofiber/chitosan/montmorillonite aerogel as adsorbent for wastewater treatment. *Sep. Purif. Technol.* **2021**, *274*, 119120. [[CrossRef](#)]
19. Xu, L.; Li, J.; Zhang, M. Adsorption characteristics of a novel carbon-nanotube-based composite adsorbent toward organic pollutants. *Ind. Eng. Chem. Res.* **2015**, *54*, 2379–2384. [[CrossRef](#)]
20. Attallah, O.A.; Al-Ghobashy, M.A.; Nebsen, M.; Salem, M.Y. Adsorptive removal of fluoroquinolones from water by pectin-functionalized magnetic nanoparticles: Process optimization using a spectrofluorimetric assay. *ACS Sustain. Chem. Eng.* **2017**, *5*, 133–145. [[CrossRef](#)]
21. Attallah, O.A.; Al-Ghobashy, M.A.; Nebsen, M.; Salem, M.Y. Removal of cationic and anionic dyes from aqueous solution with magnetite/pectin and magnetite/silica/pectin hybrid nanocomposites: Kinetic, isotherm and mechanism analysis. *RSC Adv.* **2016**, *6*, 11461–11480. [[CrossRef](#)]
22. Griggs, D.; Nilsson, M.; Stevance, A.; McCollum, D. *A Guide to SDG Interactions: From Science to Implementation*; International Council for Science: Paris, France, 2017.
23. Saheed, I.O.; Da Oh, W.; Suah, F.B.M. Chitosan modifications for adsorption of pollutants—A review. *J. Hazard. Mater.* **2021**, *408*, 124889. [[CrossRef](#)] [[PubMed](#)]
24. Okamoto, K.; Goda, T.; Yamada, T.; Nagoshi, M. Direct Ethanol Production from Xylan and Acorn Using the Starch-Fermenting Basidiomycete Fungus *Phlebia acerina*. *Fermentation* **2021**, *7*, 116. [[CrossRef](#)]
25. Mtibe, A.; Motloun, M.P.; Bandyopadhyay, J.; Ray, S.S. Synthetic biopolymers and their composites: Advantages and limitations—An overview. *Macromol. Rapid Commun.* **2021**, *42*, 2100130. [[CrossRef](#)] [[PubMed](#)]
26. Malesic-Eleftheriadou, N.; Evgenidou, E.; Lazaridou, M.; Bikiaris, D.N.; Yang, X.; Kyzas, G.Z.; Lambropoulou, D.A. Simultaneous removal of anti-inflammatory pharmaceutical compounds from an aqueous mixture with adsorption onto chitosan zwitterionic derivative. *Colloids Surf. A Physicochem. Eng. Asp.* **2021**, *619*, 126498. [[CrossRef](#)]
27. Wang, L.; Wang, A. Adsorption characteristics of Congo Red onto the chitosan/montmorillonite nanocomposite. *J. Hazard. Mater.* **2007**, *147*, 979–985. [[CrossRef](#)]
28. Mohammad, A.M.; Eldin, T.A.S.; Hassan, M.A.; El-Anadouli, B.E. Efficient treatment of lead-containing wastewater by hydroxyapatite/chitosan nanostructures. *Arab. J. Chem.* **2017**, *10*, 683–690. [[CrossRef](#)]
29. Xiang, Z.; Tang, N.; Jin, X.; Gao, W. Fabrications and applications of hemicellulose-based bio-adsorbents. *Carbohydr. Polym.* **2022**, *278*, 118945. [[CrossRef](#)]
30. Shalla, A.H.; Yaseen, Z.; Bhat, M.A.; Rangrez, T.A.; Maswal, M. Recent review for removal of metal ions by hydrogels. *Sep. Sci. Technol.* **2019**, *54*, 89–100. [[CrossRef](#)]
31. Fu, C.; Dong, X.; Wang, S.; Kong, F. Synthesis of nanocomposites using xylan and graphite oxide for remediation of cationic dyes in aqueous solutions. *Int. J. Biol. Macromol.* **2019**, *137*, 886–894. [[CrossRef](#)]
32. Ananpattarachai, J.; Kajitvichyanukul, P. Enhancement of chromium removal efficiency on adsorption and photocatalytic reduction using a bio-catalyst, titania-impregnated chitosan/xylan hybrid film. *J. Clean. Prod.* **2016**, *130*, 126–136. [[CrossRef](#)]
33. Bush, J.R.; Liang, H.; Dickinson, M.; Botchwey, E.A. Xylan hemicellulose improves chitosan hydrogel for bone tissue regeneration. *Polym. Adv. Technol.* **2016**, *27*, 1050–1055. [[CrossRef](#)]
34. Wu, S.; Hu, J.; Wei, L.; Du, Y.; Shi, X.; Deng, H.; Zhang, L. Construction of porous chitosan-xylan-TiO₂ hybrid with highly efficient sorption capability on heavy metals. *J. Environ. Chem. Eng.* **2014**, *2*, 1568–1577. [[CrossRef](#)]
35. Abu-Dief, A.M.; Mohamed, I.M. A review on versatile applications of transition metal complexes incorporating Schiff bases. *Beni-Suef Univ. J. Basic Appl. Sci.* **2015**, *4*, 119–133. [[CrossRef](#)]
36. Nnadozie, E.C.; Ajibade, P.A. Green synthesis and characterization of magnetite (Fe₃O₄) nanoparticles using *Chromolaena odorata* root extract for smart nanocomposite. *Mater. Lett.* **2020**, *263*, 127145. [[CrossRef](#)]
37. Bagbi, Y.; Sarswat, A.; Mohan, D.; Pandey, A.; Solanki, P.R. Lead (Pb²⁺) adsorption by monodispersed magnetite nanoparticles: Surface analysis and effects of solution chemistry. *J. Environ. Chem. Eng.* **2016**, *4*, 4237–4247. [[CrossRef](#)]

38. Connors, K.A. 5.5 the phenomenological theory of solvent effects in mixed solvent systems. In *Handbook of Solvents*; Chemtec Publishing: Toronto, ON, Canada, 2001; p. 281.
39. Omraei, M.; Esfandian, H.; Katal, R.; Ghorbani, M. Study of the removal of Zn (II) from aqueous solution using polypyrrole nanocomposite. *Desalination* **2011**, *271*, 248–256. [[CrossRef](#)]
40. Huang, X.; Gao, N.-y.; Zhang, Q.-l. Thermodynamics and kinetics of cadmium adsorption onto oxidized granular activated carbon. *J. Environ. Sci.* **2007**, *19*, 1287–1292. [[CrossRef](#)] [[PubMed](#)]
41. Simonin, J.-P. On the comparison of pseudo-first order and pseudo-second order rate laws in the modeling of adsorption kinetics. *Chem. Eng. J.* **2016**, *300*, 254–263. [[CrossRef](#)]
42. Ofomaja, A.E. Intraparticle diffusion process for lead (II) biosorption onto mansonia wood sawdust. *Bioresour. Technol.* **2010**, *101*, 5868–5876. [[CrossRef](#)]
43. Mostafa, A.A.; El-Sayed, M.M.; Emam, A.N.; Abd-Rabou, A.A.; Dawood, R.M.; Oudadesse, H. Bioactive glass doped with noble metal nanoparticles for bone regeneration: In vitro kinetics and proliferative impact on human bone cell line. *RSC Adv.* **2021**, *11*, 25628–25638. [[CrossRef](#)]
44. Idris, A.; Saed, K. Possible utilization of silica gel sludge for the removal of phenol from aqueous solutions: Laboratory studies. *Environmentalist* **2003**, *23*, 329–334. [[CrossRef](#)]
45. Khayyun, T.S.; Mseer, A.H. Comparison of the experimental results with the Langmuir and Freundlich models for copper removal on limestone adsorbent. *Appl. Water Sci.* **2019**, *9*, 170. [[CrossRef](#)]
46. Teleman, A.; Tenkanen, M.; Jacobs, A.; Dahlman, O. Characterization of O-acetyl-(4-O-methylglucurono) xylan isolated from birch and beech. *Carbohydr. Res.* **2002**, *337*, 373–377. [[CrossRef](#)]
47. Teleman, A.; Lundqvist, J.; Tjerneld, F.; Stållbrand, H.; Dahlman, O. Characterization of acetylated 4-O-methylglucuronoxylan isolated from aspen employing ¹H and ¹³C NMR spectroscopy. *Carbohydr. Res.* **2000**, *329*, 807–815. [[CrossRef](#)] [[PubMed](#)]
48. Schnell, C.N.; Galván, M.V.; Zanuttini, M.A.; Mocchiutti, P. Hydrogels from xylan/chitosan complexes for the controlled release of diclofenac sodium. *Cellulose* **2020**, *27*, 1465–1481. [[CrossRef](#)]
49. Gabriellii, I.; Gatenholm, P. Preparation and properties of hydrogels based on hemicellulose. *J. Appl. Polym. Sci.* **1998**, *69*, 1661–1667. [[CrossRef](#)]
50. Li, Z.; Deen, M.J.; Kumar, S.; Selvaganapathy, P.R. Raman spectroscopy for in-line water quality monitoring—Instrumentation and potential. *Sensors* **2014**, *14*, 17275–17303. [[CrossRef](#)]
51. Larkin, P. *Infrared and Raman Spectroscopy: Principles and Spectral Interpretation*; Elsevier: Amsterdam, The Netherlands, 2017.
52. Asakura, M.; Okuno, M. Hyper-Raman Spectroscopic Investigation of Amide Bands of N-Methylacetamide in Liquid/Solution Phase. *J. Phys. Chem. Lett.* **2021**, *12*, 4780–4785. [[CrossRef](#)]
53. Zajac, A.; Hanuza, J.; Wandas, M.; Dymińska, L. Determination of N-acetylation degree in chitosan using Raman spectroscopy. *Spectrochim. Acta Part A Mol. Biomol. Spectrosc.* **2015**, *134*, 114–120. [[CrossRef](#)]
54. Shen, Q.; Zhong, L.; Hu, J.-F. Characterization of the surface properties of xylan by FT-Raman spectroscopy and wicking technique. *Colloids Surf. B Biointerfaces* **2004**, *39*, 195–198. [[CrossRef](#)] [[PubMed](#)]
55. Stoia, M.; Istrate, R.; Păcurariu, C. Investigation of magnetite nanoparticles stability in air by thermal analysis and FTIR spectroscopy. *J. Therm. Anal. Calorim.* **2016**, *125*, 1185–1198. [[CrossRef](#)]
56. Unver, I.S.; Durmus, Z. Magnetic and microwave absorption properties of magnetite (Fe₃O₄)@conducting polymer (pani, ppy, pt) composites. *IEEE Trans. Magn.* **2017**, *53*, 2001708. [[CrossRef](#)]
57. Donescu, D.; Raditoiu, V.; Spataru, C.I.; Somoghi, R.; Ghiurea, M.; Radovici, C.; Fierascu, R.C.; Schinteie, G.; Leca, A.; Kuncser, V. Superparamagnetic magnetite–divinylbenzene–maleic anhydride copolymer nanocomposites obtained by dispersion polymerization. *Eur. Polym. J.* **2012**, *48*, 1709–1716. [[CrossRef](#)]
58. El-kharrag, R.; Abdel Halim, S.S.; Amin, A.; Greish, Y.E. Synthesis and characterization of chitosan-coated magnetite nanoparticles using a modified wet method for drug delivery applications. *Int. J. Polym. Mater. Polym. Biomater.* **2019**, *68*, 73–82. [[CrossRef](#)]
59. Smith, M.C.; Crist, R.M.; Clogston, J.D.; McNeil, S.E. Zeta potential: A case study of cationic, anionic, and neutral liposomes. *Anal. Bioanal. Chem.* **2017**, *409*, 5779–5787. [[CrossRef](#)]
60. Venkateswarlu, S.; Panda, A.; Kim, E.; Yoon, M. Biopolymer-coated magnetite nanoparticles and metal–organic framework ternary composites for cooperative Pb (II) adsorption. *ACS Appl. Nano Mater.* **2018**, *1*, 4198–4210. [[CrossRef](#)]
61. Predescu, A.M.; Matei, E.; Berbecaru, A.C.; Pantilimon, C.; Drăgan, C.; Vidu, R.; Predescu, C.; Kuncser, V. Synthesis and characterization of dextran-coated iron oxide nanoparticles. *R. Soc. Open Sci.* **2018**, *5*, 171525. [[CrossRef](#)]
62. Chen, S.; McClements, D.J.; Jian, L.; Han, Y.; Dai, L.; Mao, L.; Gao, Y. Core–shell biopolymer nanoparticles for co-delivery of curcumin and piperine: Sequential electrostatic deposition of hyaluronic acid and chitosan shells on the zein core. *ACS Appl. Mater. Interfaces* **2019**, *11*, 38103–38115. [[CrossRef](#)]
63. Anantha, R.K.; Kota, S. Removal of lead by adsorption with the renewable biopolymer composite of feather (*Dromaius novaehollandiae*) and chitosan (*Agaricus bisporus*). *Environ. Technol. Innov.* **2016**, *6*, 11–26. [[CrossRef](#)]
64. Zalewski, R.I. Acid–base properties of carboxylic acids, esters and amides. *Acid Deriv.* **1992**, *2*, 305–369.
65. Schnell, C.N.; Galván, M.V.; Solier, Y.N.; Inalbon, M.C.; Zanuttini, M.A.; Mocchiutti, P. High strength biobased films prepared from xylan/chitosan polyelectrolyte complexes in the presence of ethanol. *Carbohydr. Polym.* **2021**, *273*, 118602. [[CrossRef](#)] [[PubMed](#)]

66. Harrache, Z.; Abbas, M.; Aksil, T.; Trari, M. Thermodynamic and kinetics studies on adsorption of Indigo Carmine from aqueous solution by activated carbon. *Microchem. J.* **2019**, *144*, 180–189. [[CrossRef](#)]
67. Deng, J.; Lei, B.; He, A.; Zhang, X.; Ma, L.; Li, S.; Zhao, C. Toward 3D graphene oxide gels based adsorbents for high-efficient water treatment via the promotion of biopolymers. *J. Hazard. Mater.* **2013**, *263*, 467–478.
68. Bayomie, O.S.; Kandeel, H.; Shoeib, T.; Yang, H.; Youssef, N.; El-Sayed, M.M. Novel approach for effective removal of methylene blue dye from water using fava bean peel waste. *Sci. Rep.* **2020**, *10*, 7824. [[CrossRef](#)]
69. Abhari, P.S.; Manteghi, F.; Tehrani, Z. Adsorption of Lead Ions by a Green AC/HKUST-1 Nanocomposite. *Nanomaterials* **2020**, *10*, 1647. [[CrossRef](#)] [[PubMed](#)]
70. Devi, V.S.; Sudhakar, B.; Prasad, K.; Sunadh, P.J.; Krishna, M. Adsorption of Congo red from aqueous solution onto Antigonon leptopus leaf powder: Equilibrium and kinetic modeling. *Mater. Today Proc.* **2020**, *26*, 3197–3206. [[CrossRef](#)]
71. Tseng, R.-L.; Wu, F.-C. Inferring the favorable adsorption level and the concurrent multi-stage process with the Freundlich constant. *J. Hazard. Mater.* **2008**, *155*, 277–287. [[CrossRef](#)]
72. Hussain, S.; Kamran, M.; Khan, S.A.; Shaheen, K.; Shah, Z.; Suo, H.; Khan, Q.; Shah, A.B.; Rehman, W.U.; Al-Ghamdi, Y.O. Adsorption, kinetics and thermodynamics studies of methyl orange dye sequestration through chitosan composites films. *Int. J. Biol. Macromol.* **2021**, *168*, 383–394. [[CrossRef](#)]
73. An, F.; Gao, B.; Dai, X.; Wang, M.; Wang, X. Efficient removal of heavy metal ions from aqueous solution using salicylic acid type chelate adsorbent. *J. Hazard. Mater.* **2011**, *192*, 956–962. [[CrossRef](#)]
74. Li, K.; Li, P.; Cai, J.; Xiao, S.; Yang, H.; Li, A. Efficient adsorption of both methyl orange and chromium from their aqueous mixtures using a quaternary ammonium salt modified chitosan magnetic composite adsorbent. *Chemosphere* **2016**, *154*, 310–318. [[CrossRef](#)] [[PubMed](#)]
75. Weijiang, Z.; Yace, Z.; Yuvaraja, G.; Jiao, X. Adsorption of Pb (II) ions from aqueous environment using eco-friendly chitosan schiff's base@ Fe₃O₄ (CSB@ Fe₃O₄) as an adsorbent; kinetics, isotherm and thermodynamic studies. *Int. J. Biol. Macromol.* **2017**, *105*, 422–430. [[CrossRef](#)] [[PubMed](#)]
76. Li, D.; Chai, K.; Yao, X.; Zhou, L.; Wu, K.; Huang, Z.; Yan, J.; Qin, X.; Wei, W.; Ji, H. β -Cyclodextrin functionalized SBA-15 via amide linkage as a super adsorbent for rapid removal of methyl blue. *J. Colloid Interface Sci.* **2021**, *583*, 100–112. [[CrossRef](#)] [[PubMed](#)]
77. Huang, C.; Liao, H.; Ma, X.; Xiao, M.; Liu, X.; Gong, S.; Shu, X.; Zhou, X. Adsorption performance of chitosan Schiff base towards anionic dyes: Electrostatic interaction effects. *Chem. Phys. Lett.* **2021**, *780*, 138958. [[CrossRef](#)]
78. Chen, B.; Zhao, H.; Chen, S.; Long, F.; Huang, B.; Yang, B.; Pan, X. A magnetically recyclable chitosan composite adsorbent functionalized with EDTA for simultaneous capture of anionic dye and heavy metals in complex wastewater. *Chem. Eng. J.* **2019**, *356*, 69–80. [[CrossRef](#)]
79. Wang, N.; Bora, M.; Hao, S.; Tao, K.; Wu, J.; Hu, L.; Liao, J.; Lin, S.; Triantafyllou, M.S.; Li, X. Hyaluronic Acid Methacrylate Hydrogel-Modified Electrochemical Device for Adsorptive Removal of Lead (II). *Biosensors* **2022**, *12*, 714. [[CrossRef](#)]
80. Zaman Brohi, R.O.; Khuhawar, M.Y.; Mahar, R.B. Graphene oxide functionalized with a Schiff Base for the removal of Pb (II) ions from contaminated water: Experimental and modeling approach. *J. Chem. Technol. Biotechnol.* **2020**, *95*, 1694–1704. [[CrossRef](#)]
81. Essandoh, M.; Kunwar, B.; Pittman, C.U., Jr.; Mohan, D.; Mlsna, T. Sorptive removal of salicylic acid and ibuprofen from aqueous solutions using pine wood fast pyrolysis biochar. *Chem. Eng. J.* **2015**, *265*, 219–227. [[CrossRef](#)]
82. Yuan, B.; Qiu, L.-G.; Su, H.-Z.; Cao, C.-I.; Jiang, J.-h. Schiff base–Chitosan grafted l-monomuluronic acid as a novel solid-phase adsorbent for removal of congo red. *Int. J. Biol. Macromol.* **2016**, *82*, 355–360. [[CrossRef](#)]
83. Perez, T.; Pasquini, D.; de Faria Lima, A.; Rosa, E.V.; Sousa, M.H.; Cerqueira, D.A.; de Morais, L.C. Efficient removal of lead ions from water by magnetic nanosorbents based on manganese ferrite nanoparticles capped with thin layers of modified biopolymers. *J. Environ. Chem. Eng.* **2019**, *7*, 102892. [[CrossRef](#)]
84. Abdelrahman, E.A.; Hegazey, R. Utilization of waste aluminum cans in the fabrication of hydroxysodalite nanoparticles and their chitosan biopolymer composites for the removal of Ni (II) and Pb (II) ions from aqueous solutions: Kinetic, equilibrium, and reusability studies. *Microchem. J.* **2019**, *145*, 18–25. [[CrossRef](#)]
85. Lessa, E.F.; Nunes, M.L.; Fajardo, A.R. Chitosan/waste coffee-grounds composite: An efficient and eco-friendly adsorbent for removal of pharmaceutical contaminants from water. *Carbohydr. Polym.* **2018**, *189*, 257–266. [[CrossRef](#)] [[PubMed](#)]
86. Rahangdale, D.; Kumar, A. Chitosan as a substrate for simultaneous surface imprinting of salicylic acid and cadmium. *Carbohydr. Polym.* **2018**, *202*, 334–344. [[CrossRef](#)] [[PubMed](#)]
87. Annadurai, G.; Juang, R.-S.; Lee, D.-J. Use of cellulose-based wastes for adsorption of dyes from aqueous solutions. *J. Hazard. Mater.* **2002**, *92*, 263–274. [[CrossRef](#)]

Disclaimer/Publisher's Note: The statements, opinions and data contained in all publications are solely those of the individual author(s) and contributor(s) and not of MDPI and/or the editor(s). MDPI and/or the editor(s) disclaim responsibility for any injury to people or property resulting from any ideas, methods, instructions or products referred to in the content.